Radio Sources Toward Galaxy Clusters at 30 GHz

K. Coble[1,2,3], M. Bonamente[4,5], J. E. Carlstrom[3,6], K. Dawson[7], N. Hasler[5], W. Holzapfel[7], M. Joy[4], S. LaRoque[3], D. P. Marrone[8,3], E. D. Reese[9]

ABSTRACT

Extra-galactic radio sources are a significant contaminant in cosmic microwave background and Sunyaev-Zel'dovich effect experiments. Deep interferometric observations with the BIMA and OVRO arrays are used to characterize the spatial, spectral, and flux distributions of radio sources toward massive galaxy clusters at 28.5 GHz. We compute counts of mJy source fluxes from 89 fields centered on known massive galaxy clusters and 8 non-cluster fields. We find that source counts in the inner regions of the cluster fields (within 0.5 arcmin of the cluster center) are a factor of $8.9^{+4.3}_{-2.8}$ times higher than counts in the outer regions of the cluster fields (radius greater than 0.5 arcmin). Counts in the outer regions of the cluster fields are in turn a factor of $3.3^{+4.1}_{-1.8}$ greater than those in the non-cluster fields. Counts in the non-cluster fields are consistent with extrapolations from the results of other surveys. We compute spectral indices of mJy sources in cluster fields between 1.4 and 28.5 GHz and find a mean spectral index of $\alpha = 0.66$ with an rms dispersion of 0.36, where flux $S \propto \nu^{-\alpha}$. The distribution is skewed, with a median spectral index of 0.72 and 25th and 75th percentiles of 0.51 and 0.92, respectively. This is steeper than the spectral indices of stronger field sources measured by other surveys.

[1]Dept. of Chemistry and Physics, Chicago State University, 9501 South King Drive, Chicago, IL 60628, coble@oddjob.uchicago.edu

[2]NSF Astronomy and Astrophysics Postdoctoral Fellow, Adler Planetarium and Astronomy Museum

[3]Kavli Institute for Cosmological Physics, Dept. of Astronomy and Astrophysics, University of Chicago, 5640 South Ellis Ave., Chicago, IL 60637

[4]Dept. of Space Science - NSSTC, NASA Marshall Space Flight Center, Huntsville, AL 35812

[5]Dept. of Physics, University of Alabama in Huntsville, Huntsville, AL 35805

[6]Dept. of Physics, Enrico Fermi Inst., University of Chicago, 5640 South Ellis Ave., Chicago, IL 60637

[7]Dept. of Physics, University of California, Berkeley, CA 94720, (KD now at LBNL)

[8]Jansky Fellow, National Radio Astronomy Observatory

[9]Physics Department, University of California, Davis, CA

Subject headings: galaxies: clusters — cosmology: observations — cosmic microwave background — radio continuum: galaxies

1. INTRODUCTION

Extra-galactic radio sources are a significant contaminant in cosmic microwave background (CMB) and Sunyaev-Zel'dovich effect (SZE) experiments (e.g., see Holder (2002); Knox et al. (2004); Tegmark et al. (2000)). Measurements of the cosmic microwave background and of the Sunyaev-Zel'dovich effect (Sunyaev & Zel'dovich 1970, 1972) have the potential to yield a wealth of cosmological information if foreground contaminants are well-understood. Models for the number counts of radio sources as a function of flux (De Zotti et al. 2005; Toffolatti et al. 1999; Sokasian et al. 2001) have been derived from observations at lower frequencies and extrapolated to microwave frequencies.

Radio sources are often associated with the clusters of galaxies themselves. This is a potential source of bias for current and planned SZE surveys such as the Sunyaev-Zel'dovich Array (SZA)[1], Arcminute Microkelvin Imager (AMI)[2], the Atacama Pathfinder Experiment Sunyaev-Zel'dovich (APEX-SZ) survey[3], the South Pole Telescope (SPT)[4], and the Atacama Cosmology Telescope (ACT)[5]. To understand the impact on planned SZE cluster surveys, it is critical to characterize the spatial, spectral, and flux distribution of sources associated with clusters.

Contaminating radio emission from extra-galactic sources at frequencies less than approximately 100 GHz is attributed to synchrotron radiation from active galactic nuclei (AGN) and star-forming galaxies. The AGN-powered radio galaxies dominate the source counts at high luminosities. At higher frequencies, the emission is attributed to dust emission from star-forming galaxies. Observations of radio sources toward galaxy clusters at very low frequencies ($\lesssim 5$ GHz) (e.g., Slee et al. (1983, 1998); Owen (1996); Ledlow & Owen (1995); Reddy & Yun (2004)) show a strong central concentration of radio galaxies in clusters. The distribution of synchrotron-emitting star-forming galaxies is found to be less centrally-peaked in clusters (Rizza et al. 2003) than that of AGN-powered radio galaxies. At our observing

---

[1]SZA website: http://astro.uchicago.edu/sza

[2]AMI website: http://www.mrao.cam.ac.uk/telescopes/ami/

[3]APEX-SZ website: http://bolo.berkeley.edu/apexsz

[4]SPT website: http://spt.uchicago.edu/

[5]ACT website: http://www.hep.upenn.edu/act/

frequency of 28.5 GHz and sensitivity level, radio sources powered by AGN dominate and we refer to them henceforth as radio sources.

Several CMB experiments, such as WMAP (Bennett et al. 2003), DASI (Kovac et al. 2002), VSA (Cleary et al. 2005), and CBI (Mason et al. 2003), have measured microwave source counts as a function of flux for sources brighter than about 10 mJy. There have been two prior analyses of radio sources in SZE data taken with the Owens Valley Radio Observatory (OVRO)[6] and Berkeley-Illinois-Maryland Association (BIMA)[7] arrays. Using a sample of 56 fields centered on known massive galaxy clusters, Cooray et al. (1998) computed counts and spectral indices of radio sources. Using the outer regions of 41 cluster fields, LaRoque et al. (2002) computed the normalization of source counts as a function of flux for faint sources in SZE data. The data used in Cooray et al. (1998) and in LaRoque et al. (2002) are subsets of the data presented in this paper.

In this paper we analyse faint ($\sim$ mJy) radio sources found serendipitously toward massive galaxy clusters at 28.5 GHz from the OVRO/BIMA SZE imaging project. Characterizing the spatial, spectral, and flux distribution at this relatively high frequency should help improve projections for radio source contamination in SZE and CMB experiments at frequencies of 30 GHz and higher. We use 89 fields centered on known massive galaxy clusters and 8 non-cluster fields. The paper is organized as follows: Section 2 reviews the observations, data reduction, field selection, and the measured source fluxes. In Section 3, we compute spectral indices between 1.4 and 28.5 GHz using fluxes from our data and published 1.4 GHz surveys. In Section 4, we present source counts as a function of flux for cluster and non-cluster fields as well as the angular radial dependence of counts in cluster fields. We compare our results with those from other experiments and with theoretical models.

2. OBSERVATIONS

2.1. Observations

The 28.5 GHz observations were carried out with the Berkeley Illinois Maryland Association millimeter array (BIMA) during the summers of 1996 – 2002 and the Owens Valley Radio Observatory (OVRO) during the summers of 1995 – 2001 as part of the OVRO/BIMA SZE imaging project (see, for example, Reese et al. (2002) and Grego et al. (2001)). A total of 62 cluster fields were observed at BIMA and 55 cluster fields were observed at OVRO.

---

[6]The OVRO mm-wave array is operated by Caltech with support from the National Science Foundation

[7]The BIMA array is operated with support from the National Science Foundation

A total of 28 cluster fields were observed at both BIMA and OVRO, yielding observations of 89 unique cluster fields. For the BIMA CMB finescale anisotropy project (Dawson et al. 2002, 2006), a total of 18 non-cluster fields were observed.

The BIMA array consists of ten 6.1 meter diameter telescopes with primary beams of 6.6 arcmin FWHM; nine of the ten BIMA telescopes were used for the 28.5 GHz observations. The OVRO array consists of six 10.4-meter telescopes, with primary beams of 4.2 arcmin FWHM; all six OVRO telescopes were used. The primary beams were measured holographically and were found to be well-approximated by Gaussians; we use the azimuthally averaged measured beam responses in our analyses. For CMB observations at BIMA, the array was set in a compact configuration to maximize brightness sensitivity. For cluster observations at both OVRO and BIMA, most of the telescopes were also configured in a compact configuration that provided dense $u - v$ coverage to the shadowing limit, and one or two telescopes were placed at longer baselines for higher angular resolution monitoring of sources. The longest baselines used at OVRO and BIMA ranged from 70 to 140 meters for the data presented here.

The telescopes were outfitted with cm-wave receivers (Carlstrom et al. 1996) equipped with cryogenically cooled 26 - 36 GHz HEMT amplifiers (Pospieszalski et al. 1995). Typical receiver temperatures were 11 K to 20 K, and when integrated with the OVRO and BIMA telescopes yielded typical system temperatures scaled to above the atmosphere of 45 K to 55 K, and as low as 35 K. OVRO observations were correlated with an analog correlator consisting of two 1 GHz bandwidth channels centered at 28.5 and 30 GHz. The $u - v$ data from the two channels were not combined before making maps or fitting sources to the data. The OVRO correlator integration time was four minutes or less. BIMA observations were correlated with a multi-channel hybrid correlator. After calibration, the $u - v$ data were reduced to a single 0.8 GHz wide bandwidth centered at 28.5 GHz. The BIMA correlator integration time was 50 seconds.

Observations of cluster and CMB fields were interleaved every ~ 20 minutes with observations of a strong point source for phase calibration. Source data that was not bracketed in time by phase calibrator data was discarded, as was data from baselines in which one of the array elements is shadowed by another. Source data was also discarded if the bracketing phase calibrator observations showed a discontinuity in the instrument phase response. Lastly, source data was discarded if atmospheric phase fluctuations showed a loss of correlation greater than a few percent on the long baseline observations of the phase calibrator. Observations of the phase calibrators indicate the gain stability was stable to $\sim 1\%$ over several months. The absolute calibration is based on observations of Mars, with the brightness temperature taken from the Rudy (1987) model. Further details of the observations and the

data reduction can be found in Grego et al. (2001) and Reese et al. (2002).

2.2. Field Selection

The cluster fields of the OVRO/BIMA SZE imaging project were chosen to obtain precise measurements of the SZE in massive galaxy clusters. Potential targets were screened for strong radio sources using archival data at lower frequencies such as NVSS (Condon et al. 1998) and FIRST (White et al. 1997). In addition, if a strong source ($> 10 - 20$ mJy) was detected near the cluster center in the initial 28.5 GHz observations, observations ceased in favor of other less contaminated targets. Due to the constraints of this field selection, we do not attempt to characterize the distribution of sources brighter than 10 mJy in this analysis.

The cluster fields were chosen mainly from X-ray catalogs and one optical survey, including: (1) the ROSAT Brightest Cluster Survey, BCS (Ebeling et al. 1997, 1998, 2000a; Crawford et al. 1999), (2) the Einstein Observatory Extended Medium Sensitivity Survey, EMSS (Gioia et al. 1990; Stocke et al. 1991; Gioia & Luppino 1994; Maccacaro et al. 1994), (3) the ROSAT X-ray Brightest Abell Clusters, XBACS (Ebeling et al. 1996b,a), (4) the Wide Angle ROSAT Pointed Survey, WARPS (Scharf et al. 1997; Jones et al. 1998; Fairley et al. 2000; Ebeling et al. 2000b), (5) the Massive Cluster Survey, MACS (Ebeling et al. 2001a), and (6) the Red-Sequence Cluster Survey, RCS (Gladders & Yee 2005).

Clusters were selected from the BCS, EMSS, and XBACS X-ray catalogs on the basis of high X-ray luminosity. Clusters from the WARPS and MACS surveys were selected for X-ray luminosity and high redshift. The 8 clusters selected for SZE observations from the MACS survey form a complete redshift-selected flux-limited X-ray sample and were chosen regardless of possible radio source contamination (LaRoque et al. 2003). A few optically selected clusters were also provided by the RCS team. Table 1 lists the coordinates of the pointing centers for the cluster fields.

The BIMA array was also used to observe 18 non-cluster fields for CMB anisotropy measurements (Dawson et al. 2002, 2006). The pointing center coordinates for these fields are provided in Table 2. Of these fields, only the 8 fields BDF14-BDF21 (Dawson et al. 2006) were chosen without regard to possible radio source contamination. The fields BDF4, and BDF6-BDF13 (Dawson et al. 2002) were chosen from the NVSS survey to have minimal contamination from strong radio sources. The field HDF is centered on the Hubble Deep Field and was also selected to have no strong radio sources. Only the 8 fields selected without regard to source contamination are used in the analysis presented in this paper.

2.3. Source Fluxes

The positions and fluxes of 28.5 GHz sources and SZE decrements are determined using the DIFMAP software package (Pearson et al. 1994). The SZE data consist of positions in the Fourier domain (also called the $u - v$ plane) and the visibilities—the complex Fourier component pairs as functions of u and v, which are the Fourier conjugate variables to right ascension and declination. DIFMAP is used to create a map from the $u - v$ data using all baselines and natural weighting ($\propto \sigma^{-2}$). Source and decrement positions are determined from this map. Emission sources are initally assumed to be pointlike, while the SZE decrement (if any) is approximated with an elliptical, isothermal β model. The fourier transforms of the model components are jointly fit to the observed visibilities. The image of the residuals is searched for additional sources at greater than five times the image rms and any sources found in this way are added to the model and jointly refitted. Noise estimates are extracted from the final residual images.

The source fluxes determined in this way depend on the coverage of the $u - v$ plane for sources with structure on scales larger than that probed by the longest baselines (30 arcsec to 15 arcsec for the 70 to 140 meter maximum baselines employed here). To enable a uniform comparison with lower frequency data from the NVSS, which has an angular resolution of 45 arcsec, we repeat the $u - v$ fitting procedure considering only baselines shorter than 4 $k\lambda$. This provides matched angular resolution at a cost of typically $40 - 50\%$ of our data, yielding a sensitivity loss of $30 - 40\%$. We also measured the flux within an extended area centered on each radio source in the CLEANed maps made from the 4 $k\lambda$ cut and full $u - v$ data. We compared the fluxes obtained from the $u - v$ model fits and the analysis of the CLEANed maps from both the cut and full $u - v$ data. We find the fluxes found with the four methods agree for 104 out of 122 sources, double-counting sources detected with both arrays because of the difference in sensitivity and $u - v$ coverage. In these cases we conclude that the point source approximation is adequate for our angular resolution and sensitivity and we report the fluxes and noise levels determined from all baselines in Tables 1 and 2. The remaining 18 sources have best-fit point source fluxes that depend on our choice of $u - v$ range. We find, however, that the total flux recovered by the CLEAN algorithm in the region around each source in the full data set matches that obtained for the flux found with only the short baselines for all but one of these sources. In these cases we use the flux measured in the CLEANed map made from the full data set. Finally, in one case (MACS J0717.5+3745, source 1) we do not recover the full short-baseline flux when cleaning the image of the full data set. In this case we have used the flux and noise measured for just the baselines shorter than 4 $k\lambda$ for both sources in the field.

Table 1 lists the 28.5 GHz beam attenuation-corrected fluxes for sources detected in

the BIMA and OVRO cluster fields and the centroid of the SZ decrement, if any. Noise is reported for the field center in column 7, while the uncertainty in the flux of each source (column 15) properly accounts for the beam profile. The radial distance from the pointing center, or the SZ decrement if observed, to each source is also provided. At the 5σ-level or greater we detect 62 sources in the 62 BIMA cluster fields and 56 sources in the 55 OVRO cluster fields. A total of 23 sources are detected at both BIMA and OVRO, yielding 95 unique sources in the 89 cluster fields. For sources observed at both BIMA and OVRO, the flux measurements are in good agreement. Source fluxes, positions, and noise levels for the non-cluster fields are given in Table 2. We detect two sources at $\geq 5\sigma$ in the 8 BIMA non-cluster fields which were selected without regard to possible source contamination.

The fluxes in Tables 1 and 2 do not account for attenuation due to temporal and spectral averaging of the $u-v$ data, effects which are far less significant than the beam attenuation. Averaging of interferometric data in the $u-v$ plane leads to attenuation of the amplitude response as a function of angular distance from the field center that depends on the telescope array configuration. However, these effects have been restricted to insignificant levels as part of the experimental design. The bandwidth constraint translates to $\frac{\Delta\nu}{\nu} \times \frac{B}{D} < 1$, where $\frac{\Delta\nu}{\nu}$ is the fractional bandwidth, D is the diameter of an array element and B is the baseline. For the longest baselines we find values of $\frac{\Delta\nu}{\nu} \times \frac{B}{D}$ to be 0.32 - 0.64 and 0.24 - 0.47 for the BIMA and OVRO observations, respectively. For measurements using only short baselines $(< 4k\lambda)$ these values decrease to 0.18 and 0.13, respectively. The correspondence between our measured fluxes using all baselines and just the short baselines also suggests that bandwidth smearing is not important. The integration time constraint translates to $\frac{2\pi}{24}t_{int} \times \frac{B}{D} < 1$, where t_{int} is the $u-v$ averaging time in hours. For the longest baselines and integration times we find values of $\frac{2\pi}{24}t_{int} \times \frac{B}{D}$ to be less than 0.0035 and 0.001 for the BIMA and OVRO observations, respectively.

3. SPECTRAL INDICES

We use the results of surveys at lower observing frequency to constrain the spectral indices of radio sources detected with the BIMA/OVRO observations. Fluxes at 1.4 GHz are taken primarily from the NVSS catalog, which has a resolution of 45 arcsec and limiting peak source brightness of 2.5 mJy. We obtain 1.4 GHz fluxes from the FIRST catalog (limiting flux of 1 mJy and resolution of 5 arcsec) for several additional sources which were below the NVSS detection threshold. We obtain 1.4 GHz fluxes from VLA archival maps for several sources which were not in the NVSS or FIRST catalogs. Of the 95 sources in cluster fields, 88 of them have unambiguous counterparts in the NVSS, FIRST, or VLA archival

data. All 28.5 GHz sources within 0.5 arcmin of the cluster centers were confirmed to have counterparts at 1.4 GHz. The 1.4 GHz fluxes and the results of a literature search for low frequency measurements of sources not identified in the NVSS, FIRST, or VLA surveys are given in Table 1. Unless otherwise noted, the tabulated 1.4 GHz fluxes are from NVSS. For the 7 sources that do not have unambiguous 1.4 GHz counterparts in NVSS, FIRST, or the VLA archive, we assume a 1.4 GHz flux equal to three times the survey noise. In reality, the true 1.4 GHz fluxes typically will be weaker and the true spectral indices of these sources more shallow. However, because there are only 7 sources lacking 1.4 GHz detections, the bias in the resulting mean spectral index for all sources in cluster fields computed below is small. Furthermore, because the 1.4 and 28.5 GHz measurements were not made contemporaneously, variability of the sources may contribute to a broadening in the distribution of spectral indices.

We compute spectral indices between 1.4 and 28.5 GHz for sources in cluster fields (selected at 28.5 GHz) where index α is defined by $S \propto \nu^{-\alpha}$. If we use only the 88 sources with detections in NVSS, FIRST, or the VLA maps and omit the 7 sources lacking 1.4 GHz detections, the resulting mean spectral index is $\alpha = 0.66$ with an rms dispersion of 0.36. If we include limits for the 7 sources lacking 1.4 GHz detections, the mean spectral index $\alpha = 0.60$ with an rms dispersion of 0.42, and a median index of 0.71, indicating that the bias due to omitting these 7 sources is small. We use the 88 sources with NVSS, FIRST, or VLA counterparts for the remainder of our spectral index analysis. A histogram of spectral indices for these 88 sources is shown in Figure 1. Characterizations of the spectral index distribution are given in Table 3. The distribution has a tail at low-α and is not well fit by a Gaussian. We therefore also compute the median of the distribution, as well as the 25th and 75th percentiles and find them to be 0.72, 0.51, and 0.92, respectively.

While the beam attenuation factor is potentially a significant source of uncertainty for the 28.5 GHz sources, we find that excluding sources at large radius (attenuation factor greater than 5.0) does not change the results. We choose a maximum cutoff outer radius of 6.6 arcmin for BIMA and 4.2 arcmin for OVRO, corresponding to a beam attenuation factor of about 30 and spanning a region twice the FWHM of the primary beam. When a source has observations from both BIMA and OVRO, we choose the one with the best combination of sensitivity and survey area.

The radial distribution of spectral indices is shown in Figure 2; there is no apparent trend in spectral index with radius from the cluster center. We compare the spectral index distribution of the central regions of cluster fields ($r < 0.5$ arcmin) with the distribution of the outer regions of cluster fields ($r > 0.5$ arcmin) and find no significant differences. The mean spectral index for the central regions of cluster fields is $\alpha = 0.75$ with an rms dispersion

of 0.24 and the mean spectral index for the outer regions of cluster fields is $\alpha = 0.63$ with an rms dispersion of 0.38. The medians are 0.76 [0.56 (25%), 0.94 (75%)] for the central regions and 0.71 [0.42 (25%), 0.88 (75%)] for the outer regions. The results of a Kolmogorov-Smirnov (KS) test indicate that the distribution of spectral indices of sources in the inner regions of cluster fields is consistent with that of the outer regions. The maximum distance between their cumulative distribution functions is 0.18, corresponding to an 64% probability that the two samples are drawn from the same distribution. Since we have few sources in non-cluster fields, we do not compute an average spectral index for this group.

We compare the spectral index distribution of our mJy cluster sources to those of somewhat brighter field sources measured by other groups (Mason et al. 2003; Waldram et al. 2003; Bolton et al. 2004); a summary is given in Table 3. The CBI group (Mason et al. 2003) finds a spectral index from 1.4 to 31 GHz of 0.45 with an rms dispersion of 0.37. As a follow-up to the 9C survey (Waldram et al. 2003), Bolton et al. (2004) compute indices between several frequencies from 1.4 to 43 GHz, distinguishing between weak and strong sources. The mean spectral index for the lower flux sample is ~ 0.4 for the lower frequencies, and steepens to ~ 0.9 from 15.2 to 43 GHz. Waldram et al. (2003) and Bolton et al. (2004) also find a greater percentage of the strong sources have a flat or rising spectrum.

Our spectral indices are somewhat steeper than the spectral indices measured by CBI and much steeper than those of the $\sim$ Jy sources ($\alpha \sim 0$) measured by WMAP (Bennett et al. 2003). When comparing source surveys, it is essential to consider the flux and frequency at which the sources are selected. We expect a survey of strong sources selected at high frequency to have a flatter spectral index than a survey of low flux sources selected at lower frequency. Our results are for a relatively low flux survey selected at high frequency, and it is interesting that the spectral index is relatively steep. The sources in our survey primarily lie in the environments of rich galaxy clusters and it is possible that there are significant differences between this population of sources and that which is found in surveys that do not target clusters. Our spectral indices for radio sources towards clusters are similar to those found towards clusters at 2.7 GHz by Slee et al. (1983). They find that spectral indices are steeper in clusters than in the field and note a trend of shallower spectral indices with increasing cluster radius. Using our mean spectral index of 0.66, the lower flux limit of 0.12 Jy at 2.7 GHz from Slee et al. (1983) translates to 25 mJy at 28.5 GHz, which is slightly stronger than the upper limit of our source sample.

As we look at sources with higher redshift, the emission frequency of the radiation increases. We might, therefore, expect these sources to have steeper spectral indices. However, the sources are selected at higher frequency which might bias the sample toward flatter spectral indices. In Figure 3, we plot spectral index as a function of cluster redshift and see no

clear trend. The mean and rms dispersion in the spectral index are 0.67 and 0.37 for $z < 0.5$, compared to 0.64 and 0.29 for $z > 0.5$, and 0.76 and 0.20 for $z > 0.8$.

4. SOURCE COUNTS

4.1. Analysis

With the field selection effects in mind from Section 2.2, we compute the differential source counts as a function of flux, dN/dS, in several flux bins, accounting for the varying noise levels from field to field. We chose the flux bins in order to maximize the number of sources used and to have a similar number of sources in each bin.

The survey boundary of each field for a given flux bin is set by the noise level of the field. For each flux bin and field, the minimum level in the flux bin sets the allowable beam-corrected noise level and the corresponding maximum attenuation radius for the field. For example, for $\geq 5\sigma$ sources in a flux bin of 1.5 - 2.5 mJy, the allowable beam-corrected noise level is $1.5/5 = 0.3$ mJy. This noise level sets the attenuation radius for the field, the radius at which the beam attenuation factor = (beam corrected noise level)/(uncorrected noise level). We set an outer boundary on the survey area for the field using the lesser of the attenuation radius or a maximum cutoff outer radius away from the field pointing center. We choose a maximum cutoff outer radius of 6.6 arcmin for BIMA and 4.2 arcmin for OVRO, corresponding to a beam attenuation factor of about 30 and spanning a region twice the FWHM of the primary beam. We treat this as a hard maximum cutoff; even if the noise is sufficiently low to allow us to go to greater radii in our sampling of a field, we do not. The outer boundary is measured relative to the field pointing center.

We further break the data into radial bins from the cluster center. The cluster center is determined by the location of the SZE decrement. For fields without a SZE decrement detection, the pointing center is used as the center of the field. For each field, flux bin, and radial bin, we compute the survey area within the boundary set by the radial bin and the noise level for the field. Typically the survey region for a given field, flux bin, and radial bin is a circle or annulus, sometimes cut off by the noise boundary. We compute the total survey area for each flux bin by adding up the area in all the fields. When a field has observations from both BIMA and OVRO, we choose the one with the best combination of sensitivity and survey area.

For each field we identify all $\geq 5\sigma$ sources in the survey area that fall between the minimum and maximum fluxes of each flux bin. We count up the sources in each flux bin to get raw total source counts in the total survey area. The errors for the raw counts in

each bin are assumed to be Poisson distributed. Differential source counts (dN/dS) and the associated errors are calculated by dividing the total raw counts in each bin by the total survey area for the corresponding flux bin and by the flux bin width.

4.2. Results and Discussion

Differential source counts (dN/dS), the number of sources, and the survey area for each flux bin are given in Figure 4 and Table 4 for the central regions of the cluster fields (radii ≤ 0.5 arcmin), the outer regions of the cluster fields (radii ≥ 0.5 arcmin), and for the non-cluster fields. The error bars on dN/dS are the Poisson errors on the raw source counts and do not include other sources of uncertainty. Typical raw counts of sources are ~ 4 in each flux bin for the inner regions of the cluster fields and ~ 8 for the outer cluster regions. We only detect two $\geq 5\sigma$ sources in the 8 non-cluster fields that were selected without regard to possible radio source contamination.

The differential source counts can be described by a power law, $dN(S)/dS = N_0(S/S_0)^{-\gamma}$, where $S_0 = 1\,\mathrm{mJy}$ for this analysis. Best fits using a Markov chain algorithm which simultaneously estimate the normalizations for the inner, outer, non-cluster regions, and a common power law index are shown with the data in Figure 4 and are given in Table 5. The best fit common power law index is $\gamma = -1.98 \pm 0.20$. Best fit power-laws for the central and outer cluster regions individually are also shown in Figure 4 and Table 5. As a cross-check, we compute dN/dS for the BIMA and OVRO fields separately and find good agreement; see Figure 5. All uncertainties represent 68% confidence intervals unless otherwise noted.

Source counts are found to be greatly elevated toward the central core of the cluster fields. Using the normalizations from the best simultaneous fit, source counts are found to be a factor of $8.9^{+4.3}_{-2.8}$ higher in the central regions than in the outer regions of the cluster fields. Counts are also elevated in the outer regions of the cluster fields relative to the non-cluster fields by a factor of $3.3^{+4.1}_{-1.8}$. These overdensities imply that $97^{+2}_{-5}\%$ of sources in the inner regions are cluster members, as are $70^{+16}_{-37}\%$ of sources in the outer regions. A comparable overabundance of radio sources toward galaxy clusters is also seen at lower radio frequencies (e.g., Slee et al. (1983, 1998); Owen (1996); Ledlow & Owen (1995); Reddy & Yun (2004); Rizza et al. (2003)).

We considered the possibility that gravitational lensing of background radio galaxies could produce the overabundance of detected radio sources in the direction of massive galaxy clusters. A gravitational lens with magnification factor μ will modify the source counts to $dN'(S)/dS = (dN(S/\mu)/dS)/\mu^2$. If the unlensed source counts can be described by a

power law, $dN(S)/dS \propto S^{-\gamma}$, then the source counts will be changed by a factor $B = (dN'(S)/dS)/(dN(S)/dS) = \mu^{-2+\gamma}$ (Blain 2002). The mean magnification in the BIMA and OVRO cluster fields is estimated by Cooray et al. (1998) to be $\mu \sim 1.4$. In this analysis, we temporarily assume that all sources are background sources drawn from the same distribution and capable of being lensed. Using the best joint fit power law index of $\gamma = 1.98 \pm 0.20$ we expect a factor of $B = 0.99^{+0.07}_{-0.06}$, i.e., no change in source counts in the direction of the clusters due to lensing. Therefore we conclude that, regardless of the magnification, gravitational lensing can not be responsible for the significant excess of sources seen in the direction of clusters.

In Figure 6, we compare our measurements of dN/dS with the De Zotti et al. (2005) 30 GHz model and with measurements from other experiments, including WMAP, DASI, VSA, and CBI, which all examine non-cluster fields. We present source counts in terms of $log_{10}(S^{5/2}dN/dS)$, for ease of comparison. Counts in our non-cluster fields are consistent with those expected from the model and from extrapolations from other experiments, though with only two $\geq 5\sigma$ sources in those fields, the sample variance is large. The source counts toward cluster fields have a similar power law slope, but have a higher normalization than expected from extrapolations of measurements of sky not concentrated on clusters.

5. CONCLUSIONS

From deep interferometric observations at 28.5 GHz of unresolved radio sources toward 89 fields centered on massive galaxy clusters and 8 non-cluster fields, we find that differential source counts are greatly elevated in the centers of cluster fields. Counts are a factor of $8.9^{+4.3}_{-2.8}$ higher in central regions (radii ≤ 0.5 arcmin) than in the outer regions (radii ≥ 0.5 arcmin) of the cluster fields. Counts in our non-cluster fields are consistent with those expected from models and from extrapolations from other experiments. Additionally, source counts in the outer regions of cluster fields are a factor of $3.3^{+4.1}_{-1.8}$ higher than counts in non-cluster fields.

Using the NVSS and other surveys, we find a mean spectral index for sources in cluster fields between 1.4 and 28.5 GHz of $\alpha = 0.66$ with rms dispersion of 0.36, where flux $S \propto \nu^{-\alpha}$. The distribution is skewed, with a median spectral index of 0.72 [0.51 (25%), 0.92 (75%)]. This is steeper than spectral indices of stronger (~ 20 mJy) field sources, and much steeper than those of much stronger ($\sim$ Jy) field sources measured by other surveys. No significant differences are found between the distributions of the spectral indices of sources in the inner and outer regions of the clusters.

These results can be used for improving forecasts for radio source contamination of SZE

and CMB experiments. The cluster fields used in this work were chosen to contain massive clusters and the sources were identified at 28.5 GHz. We anticipate that the SZA and other instruments will be able to extend this work to less massive clusters and to sources identified at yet higher frequencies.

REFERENCES

Allen, S. W. et al. 1992, MNRAS, 259, 67

Bennett, C. L. et al. 2003, ApJS, 148, 97

Blain, A. W. 2002, MNRAS, 330, 219

Böhringer, H. et al. 2000, ApJS, 129, 435

Bolton, R. C. et al. 2004, MNRAS, 354, 485

Carlstrom, J. E., Joy, M., & Grego, L. 1996, ApJ, 456, L75

Cleary, K. A. et al. 2005, MNRAS, 360, 340

Condon, J. J., Cotton, W. D., Greisen, E. W., Yin, Q. F., Perley, R. A., Taylor, G. B., & Broderick, J. J. 1998, AJ, 115, 1693

Cooray, A. R., Grego, L., Holzapfel, W. L., Joy, M., & Carlstrom, J. E. 1998, AJ, 115, 1388

Crawford, C. S., Allen, S. W., Ebeling, H., Edge, A. C., & Fabian, A. C. 1999, MNRAS, 306, 857

Crawford, C. S., Edge, A. C., Fabian, A. C., Allen, S. W., Bohringer, H., Ebeling, H., McMahon, R. G., & Voges, W. 1995, MNRAS, 274, 75

Dahle, H., Kaiser, N., Irgens, R. J., Lilje, P. B., & Maddox, S. J. 2002, ApJS, 139, 313

Dawson, K. S., Holzapfel, W. L., Carlstrom, J. E., Joy, M., & LaRoque, S. J. 2006, ApJ, in press

Dawson, K. S., Holzapfel, W. L., Carlstrom, J. E., Joy, M., LaRoque, S. J., Miller, A. D., & Nagai, D. 2002, ApJ, 581, 86

de Zotti, G., Ricci, R., Mesa, D., Silva, L., Mazzotta, P., Toffolatti, L., & Gonzalez-Nuevo, J. 2002, A&A, 431, 893

Donahue, M., Voit, G. M., Scharf, C. A., Gioia, I. M., Mullis, C. R., Hughes, J. P., & Stocke, J. T. 1999, ApJ, 527, 525

Dressler, A., Smail, I., Poggianti, B. M., Butcher, H., Couch, W. J., Ellis, R. S., & Oemler, A. J. 1999, ApJS, 122, 51

Ebeling, H., Edge, A. C., Allen, S. W., Crawford, C. S., Fabian, A. C., & Huchra, J. P. 2000a, MNRAS, 318, 333

Ebeling, H., Edge, A. C., Bohringer, H., Allen, S. W., Crawford, C. S., Fabian, A. C., Voges, W., & Huchra, J. P. 1998, MNRAS, 301, 881

Ebeling, H., Edge, A. C., Fabian, A. C., Allen, S. W., Crawford, C. S., & Boehringer, H. 1997, ApJ, 479, L101

Ebeling, H., Edge, A. C., & Henry, J. P. 2001a, ApJ, 553, 668

Ebeling, H., Jones, L. R., Fairley, B. W., Perlman, E., Scharf, C., & Horner, D. 2001b, ApJ, 548, L23

Ebeling, H. et al. 2000b, ApJ, 534, 133

Ebeling, H., Voges, W., Bohringer, H., Edge, A. C., Huchra, J. P., & Briel, U. G. 1996a, MNRAS, 283, 1103

—. 1996b, MNRAS, 281, 799

Edge, A. C., Ebeling, H., Bremer, M., Röttgering, H., van Haarlem, M. P., Rengelink, R., & Courtney, N. J. D. 2003, MNRAS, 339, 913

Fairley, B. W., Jones, L. R., Scharf, C., Ebeling, H., Perlman, E., Horner, D., Wegner, G., & Malkan, M. 2000, MNRAS, 315, 669

Gioia, I. M., & Luppino, G. A. 1994, ApJS, 94, 583

Gioia, I. M., Maccacaro, T., Schild, R. E., Wolter, A., Stocke, J. T., Morris, S. L., & Henry, J. P. 1990, ApJS, 72, 567

Gladders, M. D., Hoekstra, H., Yee, H. K. C., Hall, P. B., & Barrientos, L. F. 2003, ApJ, 593, 48

Gladders, M. D., & Yee, H. K. C. 2005, ApJS, 157, 1

Grego, L., Carlstrom, J. E., Reese, E. D., Holder, G. P., Holzapfel, W. L., Joy, M. K., Mohr, J. J., & Patel, S. 2001, ApJ, 552, 2

Henry, J. P. et al. 1997, AJ, 114, 1293

Holder, G. P. 2002, ApJ, 580, 36

Hughes, J. P., & Birkinshaw, M. 1998, ApJ, 501, 1

Jones, L. R., Scharf, C., Ebeling, H., Perlman, E., Wegner, G., Malkan, M., & Horner, D. 1998, ApJ, 495, 100

Knox, L., Holder, G. P., & Church, S. E. 2004, ApJ, 612, 96

Kovac, J. M., Leitch, E. M., Pryke, C., Carlstrom, J. E., Halverson, N. W., & Holzapfel, W. L. 2002, Nature, 420, 772

LaRoque, S. J. et al. 2003, ApJ, 583, 559

LaRoque, S. J., Reese, E. D., Carlstrom, J. E., Holder, G., Holzapfel, W. L., Joy, M., & Grego, L. 2002, astro-ph/0204134

LaRoque, S. L., Bonamente, M., Carlstrom, J., Joy, M. K., Nagai, D., Reese, E. D., & Dawson, K. S. 2006, ApJ, 652, 917L

Ledlow, M. J., & Owen, F. N. 1995, AJ, 109, 853

Luppino, G. A., & Gioia, I. M. 1995, ApJ, 445, L77

Maccacaro, T., Wolter, A., McLean, B., Gioia, I. M., Stocke, J. T., della Ceca, R., Burg, R., & Faccini, R. 1994, Astrophys. Lett., 29, 267

Mason, B. S. et al. 2003, ApJ, 591, 540

Owen, F. N. 1996, IAUS, 175, 305

Partridge, R. B., Hilldrup, K. C., & Ratner, M. I. 1986, ApJ, 308, 46

Patel, S. K. et al. 2000, ApJ, 541, 37

Pearson, T. J. et al. 1994, BAAS, 185, 0808

Pospieszalski, M. W., Lakatosh, W. J., Nguyen, L. D., Lui, M., Liu, T., Le, M., Thompson, M. A., & Delaney, M. J. 1995, IEEE MTT-S Int. Microwave Symp., 1121

Reddy, N. A., & Yun, M. S. 2004, ApJ, 600, 695

Reese, E. D., Carlstrom, J. E., Joy, M., Mohr, J. J., Grego, L., & Holzapfel, W. L. 2002, ApJ, 581, 53

Rizza, E., Morrison, G. E., Owen, F. N., Ledlow, M. J., Burns, J. O., & Hill, J. 2003, AJ, 126, 119

Romer, A. K. et al. 2000, ApJS, 126, 209

Rudy, D. J. 1987, PhD thesis, California Institute of Technology

Scharf, C. A., Jones, L. R., Ebeling, H., Perlman, E., Malkan, M., & Wegner, G. 1997, ApJ, 477, 79

Schindler, S. et al. 1995, A&A, 299, L9

Slee, O. B., Wilson, I. R. G., & Siegman, B. C. 1983, Aust. J. Phys, 36, 101

Slee, O. B., Roy, A. L., & Andernach, H. 1998, Aust. J. Phys, 51, 971

Sokasian, A., Gawiser, E., & Smoot, G. F. 2001, ApJ, 562, 88

Stocke, J. T., Morris, S. L., Gioia, I. M., Maccacaro, T., Schild, R., Wolter, A., Fleming, T. A., & Henry, J. P. 1991, ApJS, 76, 813

Struble, M. F., & Rood, H. J. 1999, ApJS, 125, 35

Sunyaev, R. A., & Zel'dovich, Y. B. 1970, Comments Astrophys. Space Phys., 2, 66

—. 1972, Comments Astrophys. Space Phys., 4, 173

Tegmark, M., Eisenstein, D. J., Hu, W., & de Oliveira-Costa, A. 2000, ApJ, 530, 133

Toffolatti, L., De Zotti, G., Argüeso, F., & Burigana, C. 1999, in ASP Conf. Ser. 181: Microwave Foregrounds, ed. A. de Oliveira-Costa & M. Tegmark, 153

Waldram, E. M., Pooley, G. G., Grainge, K. J. B., Jones, M. E., Saunders, R. D. E., Scott, P. F., & Taylor, A. C. 2003, MNRAS, 342, 915

White, R. L., Becker, R. H., Helfand, D. J., & Gregg, M. D. 1997, ApJ, 475, 479
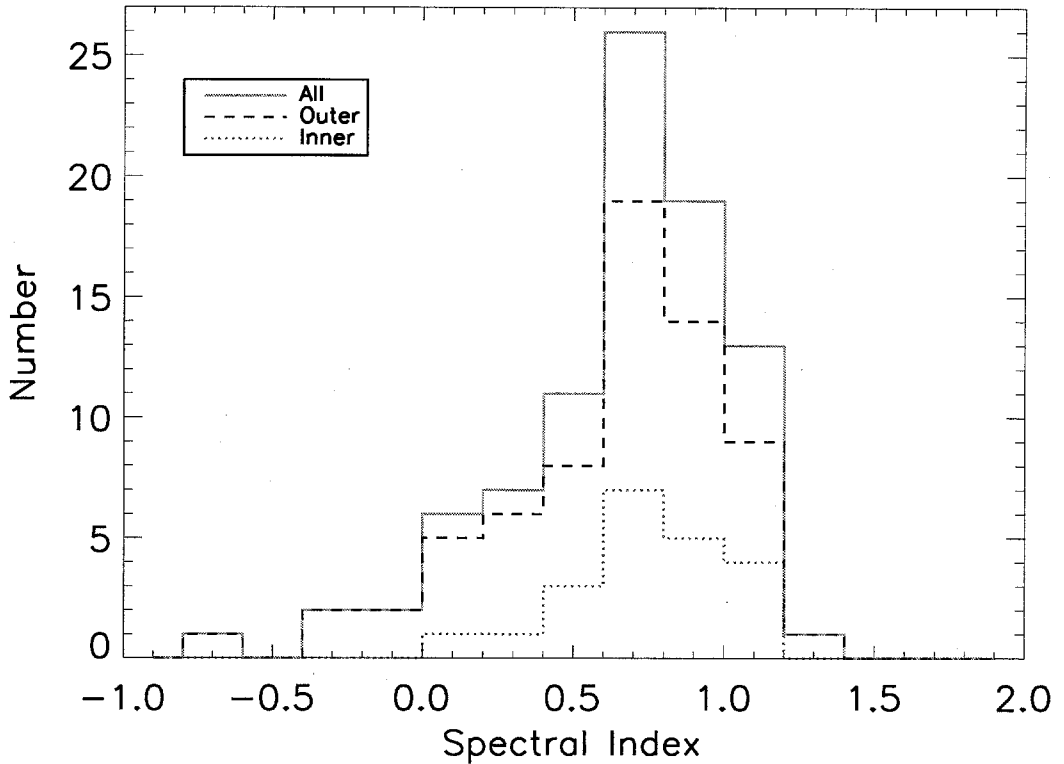
Fig. 1.— Histogram of the spectral index distribution for radio sources in cluster fields. The spectral index α is defined by $S \sim \nu^{-\alpha}$. The distribution for 88 sources is shown with a solid (green) line, the distribution for the 67 sources in the outer regions of cluster fields ($r > 0.5$ arcmin) is shown with a dashed (black) line, and the distribution for the 21 sources in the inner regions of cluster fields ($r < 0.5$ arcmin) is shown with a dotted (blue) line. The overall mean spectral index is $\alpha = 0.66$ with an rms dispersion of 0.36. The mean spectral index for the outer regions of cluster fields is $\alpha = 0.63$ with an rms dispersion of 0.38 and the mean spectral index for the the inner regions of cluster fields is $\alpha = 0.75$ with an rms dispersion of 0.24. The medians are 0.72, 0.71, and 0.76 for all, outer, and inner, respectively.
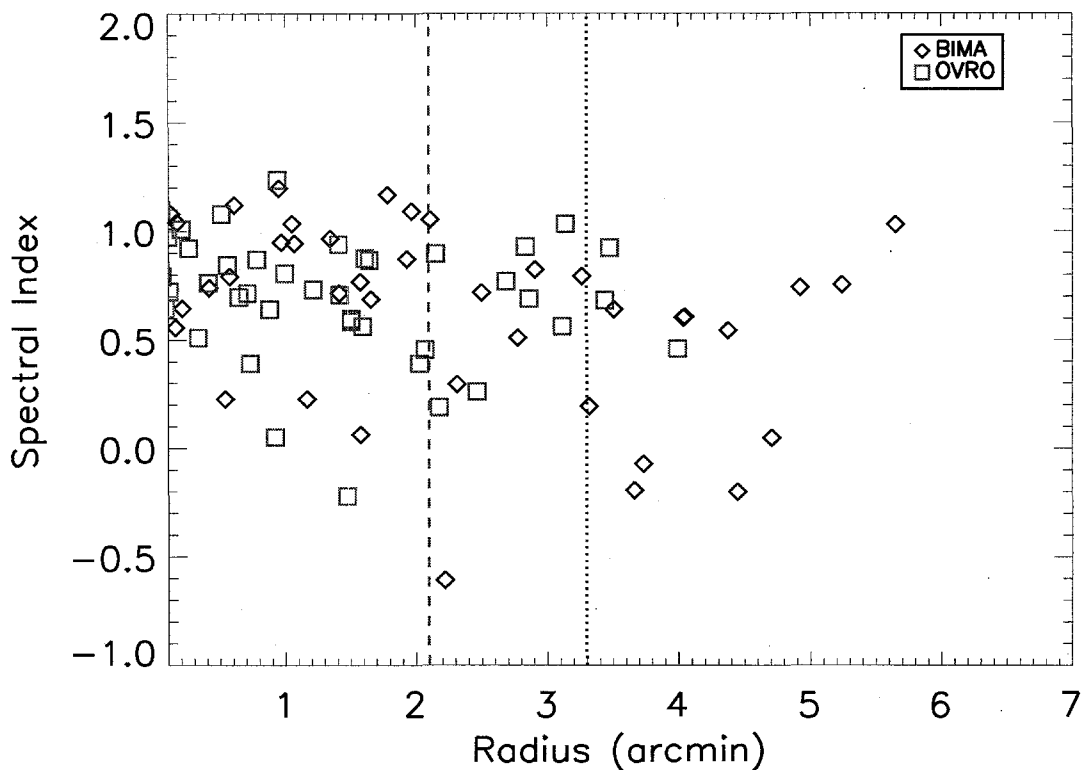
Fig. 2.— Spectral index as a function of radius for 88 cluster sources. The figure shows no clear trend with radius. The half power point for BIMA is shown as a dotted (black) line and the half power point for OVRO is shown as a dashed (blue) line. Beyond the half power point, the beam attenuation factor becomes a potentially important source of systematic uncertainty. When a source has observations from both BIMA and OVRO, we choose the field with the best combination of sensitivity and survey area; repeat sources are not shown here.
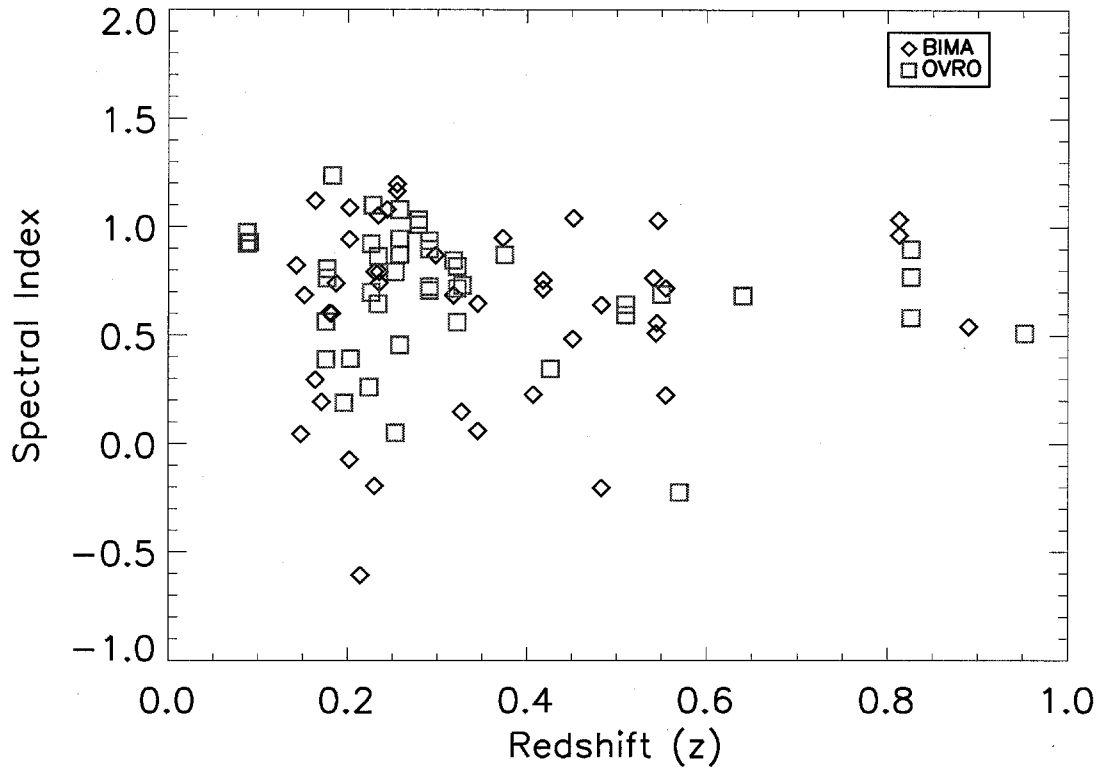
Fig. 3.— Spectral index as a function of redshift for 88 cluster sources. The figure shows no clear trend with redshift. When a source has observations from both BIMA and OVRO, we choose the field with the best combination of sensitivity and survey area; repeat sources are not shown here.
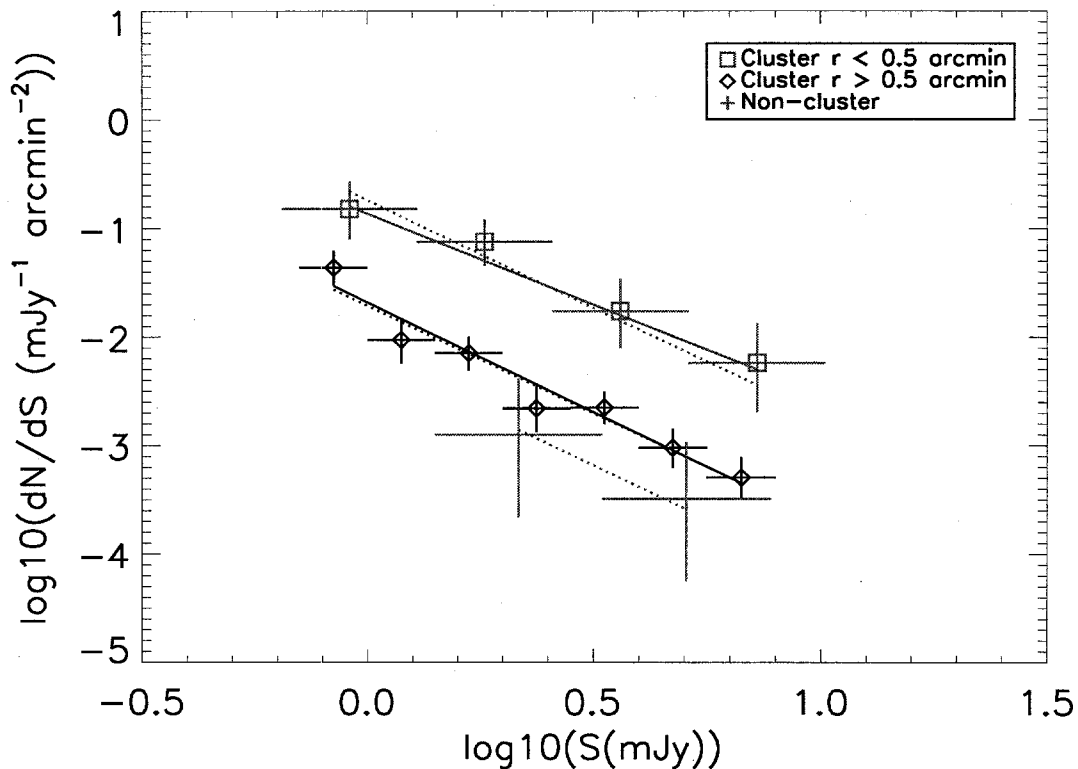
Fig. 4.— Differential number counts, $log_{10}(dN/dS)$, as a function of flux, $log_{10}(S)$, and best fit power laws for the central regions of cluster fields ($r < 0.5$ arcmin), outer regions of cluster fields ($r > 0.5$ arcmin), and non-cluster fields. Solid lines are the best fit power laws for each set individually and dotted lines are the best fits using a Markov chain algorithm to simultaneously estimate the normalizations and a common power law index. Using the best joint fit normalizations, we find that counts toward the outer regions of clusters are a factor of $3.3^{+4.1}_{-1.8}$ higher than counts in the field. Counts toward the inner regions of clusters are a factor of $8.9^{+4.3}_{-2.8}$ higher than the outer regions. The outer boundary used for the outer regions of cluster fields is set by the noise levels in the fields as described in Section 5.1. Error bars on the data come from Poisson errors on raw counts and do not include other sources of uncertainty.
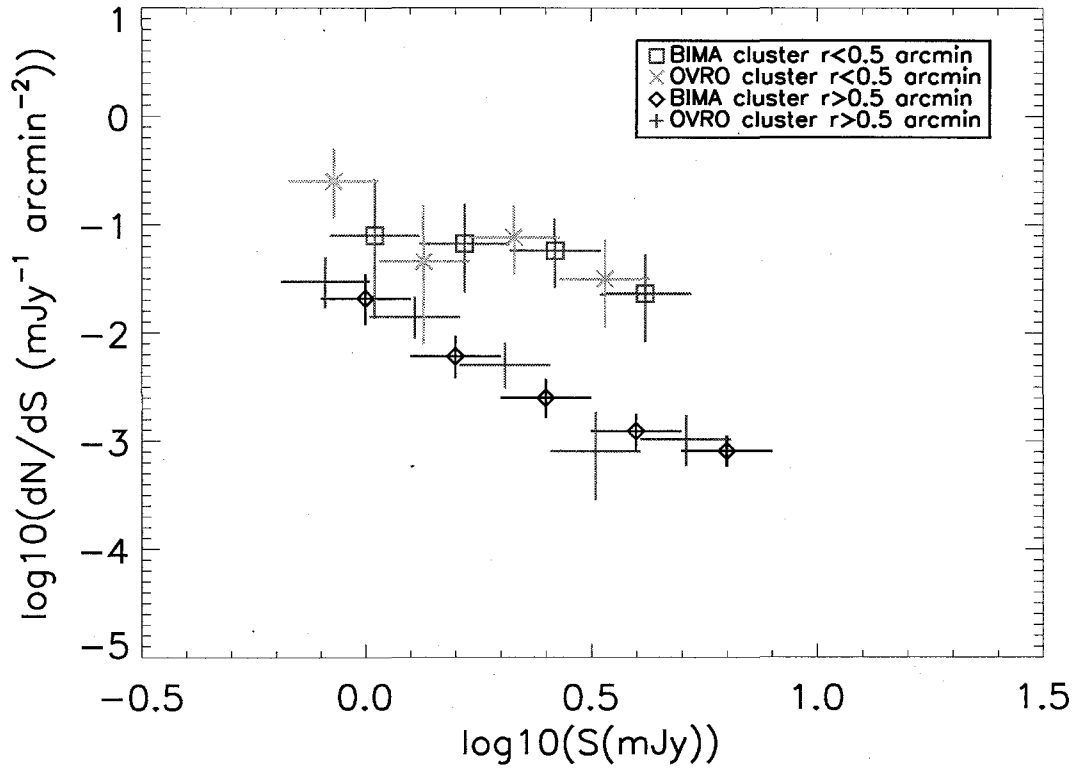
Fig. 5.— Differential number counts as a function of flux for cluster fields taken at BIMA and OVRO respectively. They are in good agreement.
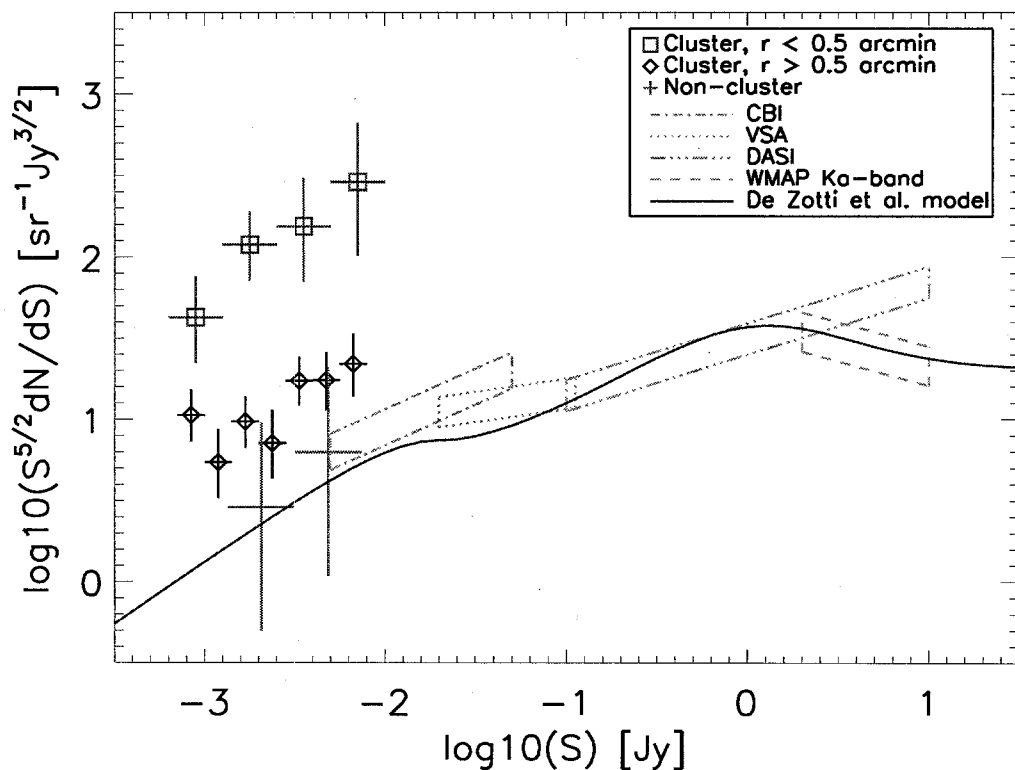
Fig. 6.— Differential number counts as a function of flux. Sources are overdense in cluster fields, especially within the central arcminute. Our SZE data are shown along with measurements from CBI (Mason et al. 2003), VSA (Cleary et al. 2005), DASI (Kovac et al. 2002), and WMAP Ka-band (Bennett et al. 2003) as well as the 30 GHz model from De Zotti et al. (2005). Counts in non-cluster fields are consistent with the model and extrapolations from other experiments.

Table 1.   Radio Sources in Cluster Fields

Field	z	ref	Pointing Center α(J2000)	Pointing Center δ(J2000)	Array	30GHz RMS (mJy)	SZ Δα(″)	SZ Δδ(″)	src	28.5 GHz Source α(J2000)	28.5 GHz Source δ(J2000)	Radius (″)	Flux (mJy)	Unc. (mJy)	1.4GHz Flux (mJy)
CL 0016+16	0.546	1	00:18:34.6	+16:26:18.2	B	0.131	-21	-14	1	00:18:31.2	+16:20:42.6	322.7	12.06	1.22	268.8
					O	0.074				· · ·	· · ·	· · ·	· · ·	· · ·	· · ·
CL J0018.8+1602	0.541	2	00:18:47.9	+16:02:22.0	B	0.180	· · ·	· · ·	1	00:18:41.4	+16:02:08.5	94.7	2.65	0.21	26.6
MACS J0025−12	0.586	3	00:22:57.8	-12:39:06.6	B	0.312	· · ·	· · ·		· · ·	· · ·	· · ·	· · ·	· · ·	· · ·
					O	0.236			1	00:22:59.9	-12:39:40.2	46.0	1.43	0.26	a
Cl 0024+1654	0.393	4	00:26:35.8	+17:09:41.0	B	0.085	· · ·	· · ·		· · ·	· · ·	· · ·	· · ·	· · ·	· · ·
Abell 68	0.255	5	00:37:06.6	+09:09:18.6	B	0.097	-17	30	1	00:37:07.6	+09:08:23.4	90.4	1.60	0.10	59.1
					B	0.097			2	00:37:07.0	+09:07:58.7	111.9	1.38	0.11	b
					B	0.097			3	00:37:06.6	+09:07:31.4	137.7	1.20	0.12	40.2
MACS J0111+08	· · ·	· · ·	01:11:34.3	+08:55:53.0	B	0.133	· · ·	· · ·		· · ·	· · ·	· · ·	· · ·	· · ·	· · ·
Abell 267	0.230	5	01:52:41.9	+01:00:24.1	B	0.101	5	2	1	01:52:54.7	+01:02:11.4	214.5	7.55	0.24	4.2
					B	0.101			2	01:52:29.2	+00:59:38.5	201.4	2.75	0.20	30.0
					O	0.073			1	01:52:54.6	+01:02:10.6	212.4	5.53	0.73	4.2
CL J0152.7−1357	0.830	6	01:52:43.0	-13:57:29.0	B	0.183	-1	-9		· · ·	· · ·	· · ·	· · ·	· · ·	· · ·
Abell 348	0.274	5	02:23:59.0	-08:35:39.4	O	0.102	· · ·	· · ·		· · ·	· · ·	· · ·	· · ·	· · ·	· · ·
RCS J0224.5−0002	0.773	7	02:24:34.1	-00:02:30.9	B	0.112	-17	-1		· · ·	· · ·	· · ·	· · ·	· · ·	· · ·
					O	0.094				· · ·	· · ·	· · ·	· · ·	· · ·	· · ·
Abell 370	0.375	5	02:39:52.5	-01:34:20.1	B	0.152	-2	-24	1	02:39:55.5	-01:34:05.6	60.3	1.18	0.16	10.5
					O	0.072			1	02:39:55.5	-01:34:06.7	59.5	0.76	0.08	10.5
Abell 383	0.187	5	02:48:03.6	-03:32:09.6	B	0.465	· · ·	· · ·	1	02:48:03.4	-03:31:44.6	25.2	4.40	0.47	48.9
MS 0302.7+1658	0.426	8	03:05:31.7	+17:10:02.8	B	0.267	· · ·	· · ·	1	03:05:31.5	+17:10:03.7	2.7	2.70	0.27	4|8
					O	0.047			1	03:05:31.7	+17:10:02.4	0.4	1.70	0.05	4|8
MACS J0329−02	0.467	9	03:29:40.5	-02:11:40.0	O	0.165	· · ·	· · ·		· · ·	· · ·	· · ·	· · ·	· · ·	· · ·
Abell 478	0.088	5	04:13:26.2	+10:27:57.6	B	0.116	-6	-9	1	04:13:25.3	+10:27:54.8	9.9	2.43	0.12	36.9
					B	0.116			2	04:13:38.3	+10:28:06.9	185.0	2.17	0.20	47.7
					O	0.059			1	04:13:26.5	+10:27:53.8	11.5	1.96	0.06	36.9
					O	0.059			2	04:13:40.3	+10:28:05.3	215.0	2.95	0.47	47.7
RX J0439.0+0715	0.244	10	04:39:01.2	+07:15:36.0	B	0.207	· · ·	· · ·	1	04:39:01.2	+07:15:28.9	7.1	1.18	0.21	30.6
MS 0451.6−0305	0.550	8	04:54:10.8	-03:00:56.8	O	0.050	11	4	1	04:54:22.1	-03:01:25.0	161.6	1.80	0.19	14.4
Abell 520	0.202	5	04:54:12.7	+02:55:23.9	B	0.103	-42	-44	1	04:54:01.1	+02:57:46.7	228.3	7.83	0.25	6.3
					B	0.103			2	04:54:16.9	+02:55:32.3	118.4	0.84	0.11	14.4
					B	0.103			3	04:54:20.3	+02:54:56.2	158.0	1.00	0.13	26.5
					O	0.078			1	04:54:01.3	+02:57:46.3	226.6	4.42	0.88	6.3
					O	0.078			2	04:54:16.8	+02:55:31.9	116.2	1.09	0.09	14.4
					O	0.078			3	04:54:20.4	+02:54:56.8	159.1	0.74	0.14	26.5
MACS J0647.7+7015	0.584	11	06:47:50.0	+70:14:55.0	O	0.061	3	1		· · ·	· · ·	· · ·	· · ·	· · ·	· · ·
MACS J0717.5+3745	0.555	12	07:17:33.8	+37:45:20.0	B	0.172	-42	0	1	07:17:37.2	+37:44:22.7	100.4	3.29	0.19	6.5[c]
					B	0.172			2	07:17:41.1	+37:43:17.5	178.0	2.28	0.25	19.8
Abell 586	0.171	5	07:32:20.3	+31:38:02.0	B	0.113	-10	-7	1	07:32:20.3	+31:41:21.0	205.9	4.42	0.23	7.9[c]
MS 0735.6+7421	0.216	8	07:41:45.0	+74:14:36.7	O	0.209	· · ·	· · ·		· · ·	· · ·	· · ·	· · ·	· · ·	· · ·
MACS J0744.8+3937	0.686	11	07:44:52.5	+39:27:30.0	B	0.241	-2	3		· · ·	· · ·	· · ·	· · ·	· · ·	· · ·
					O	0.069				· · ·	· · ·	· · ·	· · ·	· · ·	· · ·
Abell 611	0.288	5	08:00:56.7	+36:03:21.7	O	0.041	-3	1		· · ·	· · ·	· · ·	· · ·	· · ·	· · ·
Abell 665	0.182	5	08:30:59.3	+65:50:09.5	B	0.101	-11	40	1	08:31:30.8	+65:52:36.2	229.8	4.95	0.29	30.2
					O	0.076				· · ·	· · ·	· · ·	· · ·	· · ·	· · ·
Abell 697	0.282	5	08:42:57.6	+36:21:59.4	O	0.041	3	-5		· · ·	· · ·	· · ·	· · ·	· · ·	· · ·
Cl 0847.2+3617	0.373	13	08:50:10.1	+36:05:09.6	B	0.160	· · ·	· · ·	1	08:50:13.0	+36:04:22.9	58.3	1.19	0.17	20.8
Zw 2089	0.235	14	09:00:37.9	+20:54:57.6	B	0.232	· · ·	· · ·		· · ·	· · ·	· · ·	· · ·	· · ·	· · ·
Abell 750	0.180	5	09:09:11.8	+10:59:20.4	B	0.160	· · ·	· · ·	1	09:09:03.4	+11:02:50.3	243.1	3.69	0.46	22.8

Table 1—Continued

Field	z	ref	Pointing Center α(J2000)	Pointing Center δ(J2000)	Array	30GHz RMS (mJy)	SZ Δα(")	SZ Δδ(")	src	28.5 GHz Source α(J2000)	δ(J2000)	Radius (")	Flux (mJy)	Unc. (mJy)	1.4GHz Flux (mJy)
MACS J0913+40	0.452	15	09:13:46.0	+40:56:20.0	B	0.117	2	7	1	09:13:45.4	+40:56:26.7	9.5	0.69	0.12	15.9
					O	0.236				...	...	...	...	...	...
Abell 773	0.217	5	09:17:54.5	+51:43:43.5	B	0.134	-15	6		...	...	...	...	...	...
					O	0.078				...				...	...
Abell 781	0.298	5	09:20:28.8	+30:31:08.4	B	0.235	...	...	1	09:20:22.6	+30:29:44.5	116.1	5.33	0.30	73.1
Abell 851	0.407	5	09:42:56.6	+46:59:20.4	B	0.149	1	-10	1	09:42:57.5	+46:58:49.2	22.3	1.06	0.15	2.1[c]
Zwicky 2701	0.214	16	09:52:47.5	+51:53:27.6	B	0.474	...	...	1	09:52:43.1	+51:51:20.6	133.3	18.70	0.64	3.0
Abell 959	0.353	5	10:17:35.9	+59:34:05.6	O	0.089	...	...		...			...	...	...
Zwicky 3146	0.291	17	10:23:39.7	+04:11:11.0	B	0.163	5	6	1	10:23:45.0	+04:10:40.8	82.4	5.35	0.18	95.8
					B	0.163			2	10:23:37.2	+04:09:04.5	139.4	2.03	0.22	31.5
					O	0.074			1	10:23:45.0	+04:10:40.3	82.7	5.70	0.10	95.8
					O	0.074			2	10:23:37.1	+04:09:08.0	136.7	2.12	0.15	31.5
					O	0.074			3	10:23:44.9	+04:11:45.4	78.2	0.85	0.10	7.1
					O	0.074			4	10:23:39.3	+04:11:11.5	12.8	0.41	0.07	3.6
Abell 992	0.247	5	10:22:33.7	+20:29:29.8	O	0.071	...	...		...	...	...	...	...	...
Abell 990	0.144	5	10:23:39.8	+49:08:38.5	B	0.852	...	...		...	...	...	...	...	...
MS 1054.4−0321	0.826	18	10:56:59.5	-03:37:28.2	O	0.060	-5	-8	1	10:56:59.5	-03:37:26.9	11.0	0.94	0.06	14.1
					O	0.060			2	10:56:48.8	-03:37:26.5	156.3	1.79	0.19	18.2
					O	0.060			3	10:56:57.9	-03:38:55.2	81.2	0.54	0.08	3.1|
MACS J1108+09	0.480	19	11:08:55.5	+09:06:00.0	O	0.113	...	...		...	...	...	...	...	...
MACS J1115+53	0.510	20	11:15:14.9	+53:19:56.0	O	0.077	-4	14	1	11:15:17.2	+53:19:07.3	67.1	1.06	0.09	7.3
					O	0.077			2	11:15:21.3	+53:18:46.0	103.7	0.75	0.11	4.5
Zwicky 5247	0.229	21	12:34:17.3	+09:46:12.0	B	0.379	...	...		...	...	...	...	...	...
MS 1137+66	0.782	22	11:40:23.9	+66:08:19.1	B	0.081	-12	-14		...	...	...	...	...	...
Abell 1351	0.322	5	11:42:24.6	+58:32:06.5	O	0.122	...	...	1	11:42:24.4	+58:32:04.5	2.4	6.37	0.12	74.6[c]
					O	0.122			2	11:42:13.7	+58:31:23.3	95.9	1.86	0.18	10.0[c]
					O	0.122			3	11:42:22.9	+58:31:25.9	42.7	0.84	0.13	7.2[c]
MACS J1149.5+2223	0.544	11	11:49:34.3	+22:23:42.5	B	0.113	10	12	1	11:49:22.3	+22:23:29.2	177.4	3.40	0.18	15.8
					O	0.243				...	...	...	...	...	...
Abell 1413	0.143	5	11:55:18.0	+23:24:18.9	B	0.146	-4	21	1	11:55:08.7	+23:26:17.0	158.0	2.36	0.25	28.1
CL 1226+33	0.890	23	12:26:58.0	+33:32:45.0	B	0.116	1	13	1	12:27:18.8	+33:32:06.0	264.4	5.83	0.41	29.8
Abell 1576	0.279	5	12:36:59.3	+63:11:10.3	O	0.102	...	...	1	12:36:57.6	+63:11:11.7	12.0	0.88	0.10	18.4
					O	0.102			2	12:36:32.4	+63:11:58.6	188.4	2.93	0.52	65.9
Abell 1682	0.234	5	13:06:57.2	+46:32:42.0	B	0.422	...	...	1	13:06:45.9	+46:33:30.7	126.7	8.10	0.55	193.6
MACS J1311.0−0311	0.519	24	13:11:01.7	-03:10:39.0	B	0.123	9	-6		...	...	...	...	...	...
Abell 1689	0.183	5	13:11:30.3	-01:20:25.4	B	0.169	-18	-4	1	13:11:31.2	-01:19:34.5	63.2	1.30	0.18	59.6
					O	0.059			1	13:11:31.5	-01:19:32.0	67.9	1.43	0.07	59.6
Abell 1703	0.258	5	13:15:05.3	+51:49:01.9	O	0.243	...	...	1	13:15:08.5	+51:48:53.7	30.7	1.74	0.25	45.0
Abell 1704	0.221	5	13:14:26.0	+64:34:41.2	O	0.098	...	...		...	...	...	...	...	...
Abell 1722	0.328	5	13:20:09.1	+70:04:38.6	O	0.124	...	...	1	13:20:14.6	+70:05:46.2	73.0	0.93	0.15	8.4
RCS J1324.5+2844	0.997	25	13:24:28.3	+28:44:58.5	O	0.065	...	...		...	...	...	...	...	...
RCS J1326.5+2903	0.952	25	13:26:31.1	+29:03:19.8	B	0.140	-4	-15		...	...	...	...	...	...
					O	0.065			1	13:26:31.9	+29:03:36.5	34.8	0.60	0.07	2.8
Abell 1763	0.228	5	13:35:20.2	+41:00:04.0	O	0.407	...	...	1	13:35:20.0	+41:00:02.3	2.6	31.20	0.41	857.2
RX J1347.5−1145	0.451	26	13:47:30.7	-11:45:08.6	B	0.188	-2	4	1	13:47:30.6	-11:45:09.2	4.5	10.68	0.19	45.9
					O	0.235			1	13:47:30.6	-11:45:07.7	2.9	9.93	0.23	45.9
MS 1358.4+6245	0.327	8	13:59:50.6	+62:31:05.3	B	0.084	-6	2	1	13:59:50.7	+62:31:05.6	6.6	1.67	0.08	2.6[c]
					O	0.089			1	13:59:50.6	+62:31:04.6	6.5	1.51	0.09	2.6[c]
Abell 1835	0.253	5	14:01:02.0	+02:52:41.7	B	0.137	-3	4	1	14:01:02.1	+02:52:43.0	4.3	3.31	0.14	31.2[c]

Table 1—Continued

Field	z	ref	Pointing Center α(J2000)	δ(J2000)	Array	30GHz RMS (mJy)	SZ Δα('')	Δδ('')	src	28.5 GHz Source α(J2000)	δ(J2000)	Radius (")	Flux (mJy)	Unc. (mJy)	1.4GHz Flux (mJy)
					B	0.137			2	14:01:00.4	+02:51:51.0	58.6	1.26	0.14	1.6[c]
					O	0.073			1	14:01:02.1	+02:52:44.5	4.6	2.88	0.07	31.2[c]
					O	0.073			2	14:01:00.5	+02:51:51.2	57.7	1.36	0.08	1.6[c]
RCS J1419.2+5326	0.640	7	14:19:12.1	+53:26:11.4	O	0.117	...	...	1	14:19:24.2	+53:23:15.5	206.4	15.66	0.89	122.3
MACS J1423.8+2404	0.545	11	14:23:48.3	+24:04:47.5	B	0.121	-9	-10	1	14:23:47.7	+24:04:43.1	5.9	1.49	0.12	8.0
Abell 1914	0.171	5	14:26:03.5	+37:49:46.5	B	0.150	-32	-8		...	...	...	...	...	...
Abell 1995	0.318	27	14:52:57.6	+58:02:55.7	B	0.096	7	1	1	14:52:47.5	+58:01:56.1	106.1	0.62	0.11	4.9
					O	0.051			2	14:53:00.6	+58:03:19.4	27.9	0.60	0.05	7.7
MS 1455.0+2232	0.258	8	13:15:05.3	+51:49:01.9	B	0.321			1	14:56:59.3	+22:18:59.2	239.0	6.35	0.89	19.3
					O	0.037			1	14:56:59.2	+22:19:01.1	239.5	4.88	0.69	19.3
					O	0.037			2	14:57:15.1	+22:20:34.8	0.7	0.96	0.04	16.5
					O	0.037			3	14:57:08.3	+22:20:14.7	96.8	0.95	0.05	13.2
					O	0.037			4	14:57:10.8	+22:18:45.6	124.1	0.99	0.07	3.9
RX J1532.9+3021	0.345	14	15:32:54.2	+30:21:10.8	B	0.176	34	-8	1	15:32:50.9	+30:19:46.2	108.3	6.58	0.20	7.9
					B	0.176			2	15:32:53.8	+30:20:59.4	39.2	3.25	0.18	22.8
Abell 2111	0.229	5	15:39:41.8	+34:25:01.2	B	0.091	-23	1		...	...	...	...	...	...
Abell 2142	0.091	5	15:58:20.2	+27:13:52.0	B	0.159	17	20	1	15:58:14.1	+27:16:20.2	161.9	7.81	0.26	107.3
					O	0.063			1	15:58:14.1	+27:16:21.5	163.2	6.54	0.23	107.3
Abell 2146	0.234	5	15:56:14.4	+66:20:56.2	O	0.148	...	...	1	15:56:13.8	+66:20:53.5	4.5	2.19	0.15	15.3
					O	0.148			2	15:56:04.2	+66:22:13.9	98.8	3.01	0.22	40.6
					O	0.148			3	15:55:58.0	+66:20:04.4	111.4	1.43	0.25	
Abell 2163	0.203	5	16:15:46.0	-06:08:55.0	B	0.169	38	8	1	16:15:43.6	-06:08:42.3	74.5	1.31	0.17	4.8[e]
					O	0.071			1	16:15:43.3	-06:08:40.5	79.0	1.47	0.08	4.8[e]
RCS J1620.2+2929	0.870	7	16:20:10.0	+29:29:21.5	O	0.106	...	...		...	...	...	...	...	...
MACS J1621.3+3810	0.465	12	16:21:24.0	+28:10:02.0	B	0.127	26	1		...	...	...	...	...	...
					O	0.089				...	...	...	...	...	...
Abell 2204	0.152	5	16:32:46.9	+05:34:32.4	B	0.129	-7	-11	1	16:32:47.0	+05:34:33.2	14.4	8.79	0.13	69.3
Abell 2218	0.176	5	16:35:49.5	+66:12:44.4	B	0.124	12	-16	1	16:35:22.3	+66:13:20.4	183.8	5.17	0.20	f
					B	0.124			2	16:36:15.0	+66:14:23.6	183.2	3.09	0.22	12.1[e]
					B	0.124			3	16:35:47.6	+66:14:44.6	138.4	1.41	0.16	4.8[e]
					O	0.054			1	16:35:22.1	+66:13:22.2	185.6	4.45	0.20	f
					O	0.054			2	16:36:15.8	+66:14:22.3	186.5	2.22	0.27	12.1[e]
					O	0.054			3	16:35:47.7	+66:14:45.6	139.3	1.49	0.10	4.8[e]
Abell 2219	0.226	5	16:40:20.7	+46:42:39.8	O	0.165	...	...	1	16:40:22.0	+46:42:47.0	15.4	14.87	0.17	239.1
					O	0.165			2	16:40:23.6	+46:42:15.3	38.9	0.97	0.17	7.9
RXJ 1716+67	0.813	28	17:16:49.2	+67:08:23.5	B	0.109	30	-34	1	17:16:38.4	+67:08:20.5	98.2	6.60	0.12	149.6
					B	0.109			2	17:16:35.6	+67:08:39.1	120.1	5.24	0.12	95.6
					B	0.109			3	17:16:52.1	+67:08:53.9	65.7	0.75	-0.11	g
RX J1720.1+2637	0.164	10	17:20:08.9	+26:38:06.0	B	0.167	...	...	1	17:20:09.9	+26:37:32.1	36.6	2.99	0.17	87.7
					B	0.167			2	17:20:01.1	+26:36:34.7	138.7	1.68	0.23	4.1
Abell 2259	0.164	5	17:20:09.7	+27:40:08.4	B	0.131	-10	1		...	...	...	...	...	...
Abell 2261	0.224	5	17:22:27.1	+32:07:58.6	B	0.154	-3	1	1	17:22:17.0	+32:09:12.6	144.8	9.32	0.22	23.0
					O	0.062			1	17:22:17.1	+32:09:14.1	144.8	10.48	0.16	23.0
Abell 2294	0.178	5	17:23:55.3	+85:53:24.0	B	0.345	...	...		...	...	...	...	...	...
MS 2053.7-0449	0.583	8	20:56:21.8	-04:37:51.6	O	0.031	-13	-4		...	...	...	...	...	...
Abell 2345	0.177	5	21:27:13.6	-12:09:45.4	O	0.194	...	...	1	21:27:09.7	-12:10:00.9	59.9	5.07	0.22	57.6[e]
					O	0.194			2	21:27:12.0	-12:09:49.5	24.8	3.84	0.20	38.2[e]
MACS J2129.4-0741	0.570	11	21:29:26.0	-07:41:28.0	O	0.069	-16	-4	1	21:29:30.2	-07:42:30.2	98.0	1.18	0.10	0.6[h]
RX J2129.6+0005	0.235	10	21:29:37.9	+00:05:38.4	B	0.095	30	-26	1	21:29:39.9	+00:05:21.8	9.4	2.33	0.10	25.4

Table 1—Continued

Field	z	ref	Pointing Center α(J2000)	δ(J2000)	Array	30GHz RMS (mJy)	SZ Δα(")	Δδ(")	src	28.5 GHz Source α(J2000)	δ(J2000)	Radius (")	Flux (mJy)	Unc. (mJy)	1.4GHz Flux (mJy)
					B	0.095			2	21:29:55.1	+00:08:01.7	284.2	3.68	0.48	34.3
Abell 2409	0.148	5	22:00:54.5	+20:57:32.4	B	0.106	-18	34	1	22:01:11.3	+20:54:55.6	316.4	3.40	0.46	3.9
					B	0.106			2	22:01:18.0	+20:57:51.9	346.9	4.47	0.85	i
MACS J2214.9−1359	0.483	29	22:14:57.5	-14:00:15.0	B	0.159	14	4	1	22:14:39.4	-14:00:58.2	281.6	107.1	0.58	58.0
					B	0.159			2	22:14:59.2	-13:56:45.8	205.4	3.51	0.35	24.2
					O	0.128				. . .	. . .	. . .	. . .	. . .	. . .
MACS J2228.5+2036	0.418	30	22:28:34.4	+20:36:37.0	B	0.110	-20	37	1	22:28:32.6	+20:35:15.7	118.6	0.84	0.12	7.2
					B	0.110			2	22:28:28.5	+20:31:33.3	346.6	5.21	0.72	50.4
MACS J2243.3−0935	0.444	31	22:43:21.0	-09:35:25.0	B	0.618	-35	12		. . .	. . .	. . .	. . .	. . .	. . .
					O	0.121			1	22:43:17.8	-09:35:08.4	12.5	0.93	0.13	j
Abell 2507	0.196	5	22:56:51.6	+05:30:12.2	O	0.072	. . .	. . .	1	22:56:44.0	+05:31:15.5	130.5	8.15	0.15	14.4

[a]No detection found in the literature. Using the 3 times the NVSS noise level, we set an upper limit on the 1.4 GHz flux of 1.35 mJy and an upper limit on the 1.4 to 28.5 GHz spectral index of 0.0.

[b]No detection found in the literature. Using the 3 times the NVSS noise level, we set an upper limit on the 1.4 GHz flux of 1.35 mJy and an upper limit on the 1.4 to 28.5 GHz spectral index of 0.0.

[c]FIRST catalog.

[d]No detection found in the literature. Using the 3 times the NVSS noise level, we set an upper limit on the 1.4 GHz flux of 1.35 mJy and an upper limit on the 1.4 to 28.5 GHz spectral index of 0.0.

[e]VLA map. Fluxes are obtained by CLEANing the images in AIPS.

[f]Using the 3 times the VLA map noise level, we set an upper limit on the 1.4 GHz flux of 0.45 mJy and an upper limit on the 1.4 to 28.5 GHz spectral index of -0.7. The source is detected at 6 cm by Partridge et al. (1986) with a flux of 2.59 mJy, which yields a spectral index of -0.4 from 5 to 28.5 GHz.

[g]No detection found in the literature. Using the 3 times the VLA map noise level, we set an upper limit on the 1.4 GHz flux of 1.32 mJy and an upper limit on the 1.4 to 28.5 GHz spectral index of +0.2.

[h]FIRST map.

[i]No detection. Using the 3 times the NVSS noise level, we set an upper limit on the 1.4 GHz flux of 1.35 mJy and an upper limit on the 1.4 to 28.5 GHz spectral index of -0.4.

[j]No detection. Using the 3 times the FIRST noise level, we set an upper limit on the 1.4 GHz flux of 0.45 mJy and an upper limit on the 1.4 to 28.5 GHz spectral index of -0.4.

Note. — References:

1. Stocke et al. (1991)

2. Hughes & Birkinshaw (1998)

3. From Chandra X-ray spectrum (observations 3521+5010, 45 ksec exposure) we obtain $z = 0.586 \pm 0.01$.

4. Dressler et al. (1999)

5. Struble & Rood (1999)

6. Romer et al. (2000)

7. Gladders et al. (2003)

8. Gioia & Luppino (1994)

9. From Chandra X-ray spectrum (observations 3257+3582+6108, 70 ksec exposure) we obtain $z = 0.467 \pm 0.005$.

10. Ebeling et al. (1998)

11. LaRoque et al. (2003)

12. Edge et al. (2003)

13. Crawford et al. (1999)

14. Dahle et al. (2002)

15. From Chandra X-ray spectrum (observation 509, 10 ksec exposure) we obtain $z = 0.452 \pm 0.005$.

16. Crawford et al. (1995)

17. Allen et al. (1992)

18. Luppino & Gioia (1995)

19. From Chandra X-ray spectrum (observations 3252+5009, 35 ksec exposure) we obtain $z = 0.48^{+0.03}_{-0.06}$.

20. From Chandra X-ray spectrum (observations 3253+5008+5350, 35 ksec exposure) we obtain $z = 0.51^{+0.04}_{-0.05}$.

21. Böhringer et al. (2000)

22. Donahue et al. (1999)

23. Ebeling et al. (2001b)

24. From Chandra X-ray spectrum (observations 3258+6110, 85 ksec exposure) we obtain $z = 0.519 \pm 0.007$.

25. Gladders & Yee (2005)

26. Schindler et al. (1995)

27. Patel et al. (2000)

28. Henry et al. (1997)

29. LaRoque et al. (2006)

30. From Chandra X-ray spectrum (observation 3285, 20 ksec exposure) we obtain $z = 0.42^{+0.01}_{-0.02}$.

31. From Chandra X-ray spectrum (observation 3260, 21 ksec exposure) we obtain $z = 0.44 \pm 0.01$.

Table 2.   Radio Sources in Non-Cluster Fields.

Field	Pointing Center α(J2000)	Pointing Center δ(J2000)	30GHz RMS (mJy)	28.5 GHz Source α(J2000)	28.5 GHz Source δ(J2000)	Radius (")	Flux (mJy)	Unc. (mJy)	1.4GHz Flux (mJy)
BDF4	00:28:04.4	+28:23:06.0	0.075	. . .	. . .	. . .	. . .	. . .	. . .
BDF4	00:28:04.4	+28:23:06.0	0.115	. . .	. . .	. . .	. . .	. . .	. . .
HDF	12:36:49.4	+62:12:58.0	0.084	12:36:45.7	+62:11:30.2	91.5	0.48	0.10	0.00
BDF6	18:21:00.0	+59:15:00.0	0.074	. . .	. . .	. . .	. . .	. . .	. . .
BDF6	18:21:00.0	+59:15:00.0	0.059	. . .	. . .	. . .	. . .	. . .	. . .
BDF7	06:58:45.0	+55:17:00.0	0.083	. . .	. . .	. . .	. . .	. . .	. . .
BDF8	00:17:30.0	+29:00:00.0	0.071	. . .	. . .	. . .	. . .	. . .	. . .
BDF9	12:50:15.0	+56:52:30.0	0.084	. . .	. . .	. . .	. . .	. . .	. . .
BDF10	18:12:37.2	+58:32:00.0	0.086	18:12:16.6	+58:29:10.1	234.2	1.54	0.23	0.00
BDF11	06:58:00.0	+54:24:00.0	0.090	. . .	. . .	. . .	. . .	. . .	. . .
BDF12	06:57:38.0	+55:32:00.0	0.104	. . .	. . .	. . .	. . .	. . .	. . .
BDF13	22:22:45.0	+36:37:00.0	0.097	. . .	. . .	. . .	. . .	. . .	. . .
BDF14	00:26:04.4	+28:23:06.0	0.093	. . .	. . .	. . .	. . .	. . .	. . .
BDF15	06:56:45.0	+55:17:00.0	0.076	06:56:44.0	+55:11:38.4	321.7	7.07	0.55	4.50
BDF16	12:34:49.4	+62:12:58.0	0.092	. . .	. . .	. . .	. . .	. . .	. . .
BDF17	18:19:00.0	+59:15:00.0	0.090	. . .	. . .	. . .	. . .	. . .	. . .
BDF18	00:15:30.0	+29:00:00.0	0.087	. . .	. . .	. . .	. . .	. . .	. . .
BDF19	06:55:38.0	+55:32:00.0	0.084	. . .	. . .	. . .	. . .	. . .	. . .
BDF20	12:48:15.0	+56:52:30.0	0.088	12:48:45.2	+56:52:46.0	247.7	1.36	0.27	4.30
BDF21	18:10:37.2	+58:32:00.0	0.083	. . .	. . .	. . .	. . .	. . .	. . .

Table 3. Spectral indices.

Data Set	Frequency Range	No. Sources	Mean Index ± RMS	Median Index [25%, 75%]	Flux Limits
Overall cluster ($r \geq 0.5$ arcmin)	1.4 to 28.5 GHz	88	0.66 ± 0.36	0.72 [0.51, 0.92]	∼ 0.6 - 10.0 mJy at 28.5 GHz (see text)
Inner cluster ($r \leq 0.5$ arcmin)	1.4 to 28.5 GHz	21	0.75 ± 0.24	0.76 [0.56, 0.94]	∼ 0.6 - 10.0 mJy at 28.5 GHz (see text)
Outer cluster ($r \geq 0.5$ arcmin)	1.4 to 28.5 GHz	67	0.63 ± 0.38	0.71 [0.42, 0.88]	∼ 0.7 - 8.0 mJy at 28.5 GHz (see text)
Mason et al. 2003 (CBI)	1.4 to 31 GHz	56	0.45 ± 0.37	⋯	21 mJy at 31 GHz
Bolton et al. 2004 (9C follow-up)	1.4 to 4.8 GHz	124	⋯	0.44 [0.05, 0.76]	25 mJy at 15.2 GHz
Bolton et al. 2004 (9C follow-up)	4.8 to 15.2 GHz	124	⋯	0.39 [0.06, 0.95]	25 mJy at 15.2 GHz
Bolton et al. 2004 (9C follow-up)	15.2 to 43 GHz	124	⋯	0.87 [0.42, 1.20]	25 mJy at 15.2 GHz
Bolton et al. 2004 (9C follow-up)	1.4 to 4.8 GHz	70	⋯	0.24 [−0.12, 0.64]	60 mJy at 15.2 GHz
Bolton et al. 2004 (9C follow-up)	4.8 to 15.2 GHz	70	⋯	0.27 [0.02, 0.70]	60 mJy at 15.2 GHz
Bolton et al. 2004 (9C follow-up)	15.2 to 43 GHz	70	⋯	0.67 [0.38, 1.03]	60 mJy at 15.2 GHz

Table 4.   Number counts for $\geq 5\sigma$ sources at 28.5 GHz.

log10(S) (mJy)	radius range (arcmin)[a]	raw counts	area (arcmin^2)	$log_{10}(dN/dS)$ (arcmin^{-2} mJy^{-1})	field type
−0.15 : 0.00	≥ 0.5	10	783	$-1.35^{+0.15}_{-0.16}$	cluster
0.00 : 0.15	≥ 0.5	6	1541	$-2.03^{+0.20}_{-0.22}$	cluster
0.15 : 0.30	≥ 0.5	10	2420	$-2.15^{+0.15}_{-0.15}$	cluster
0.30 : 0.45	≥ 0.5	6	3306	$-2.66^{+0.20}_{-0.22}$	cluster
0.45 : 0.60	≥ 0.5	11	4217	$-2.65^{+0.15}_{-0.15}$	cluster
0.60 : 0.75	≥ 0.5	8	5104	$-3.02^{+0.17}_{-0.18}$	cluster
0.75 : 0.90	≥ 0.5	7	5951	$-3.29^{+0.19}_{-0.20}$	cluster
−0.20 : 0.10	≤ 0.5	4	42.0	$-0.82^{+0.25}_{-0.28}$	cluster
0.10 : 0.40	≤ 0.5	6	63.4	$-1.12^{+0.20}_{-0.22}$	cluster
0.40 : 0.70	≤ 0.5	3	69.0	$-1.76^{+0.30}_{-0.34}$	cluster
0.70 : 1.00	≤ 0.5	2	69.5	$-2.24^{+0.37}_{-0.45}$	cluster
0.13 : 0.50	≥ 0.0	1	438	$-2.90^{+0.52}_{-0.76}$	non-cluster
0.50 : 0.87	≥ 0.0	1	724	$-3.49^{+0.52}_{-0.76}$	non-cluster

[a]Max radius varies for individual fields since set by noise. See text.

Table 5.   Power law fits to dN/dS.

Field type	Best indiv. fit index	Best indiv. fit normalization	Best joint fit index	Best joint fit normalization
Inner cluster ($r \leq 0.5$ arcmin)	-1.67 ± 0.37	$132^{+108}_{-41} \times 10^{-3}$ mJy^{-1} arcmin^{-2}	-1.98 ± 0.20	$174^{+60}_{-45} \times 10^{-3}$ mJy^{-1} arcmin^{-2}
Outer cluster ($r \geq 0.5$ arcmin)	-2.02 ± 0.22	$20.9^{+5.4}_{-4.3} \times 10^{-3}$ mJy^{-1} arcmin^{-2}	-1.98 ± 0.20	$19.5^{+4.0}_{-5.0} \times 10^{-3}$ mJy^{-1} arcmin^{-2}
Non-cluster	$\cdots$	$\cdots$	-1.98 ± 0.20	$5.90^{+6.70}_{-3.15} \times 10^{-3}$ mJy^{-1} arcmin^{-2}